J. Mech. Phys. Solids 99 (2017) 19–34

Contents lists available at ScienceDirect

Journal of the Mechanics and Physics of Solids

journal homepage: www.elsevier.com/locate/jmps

Elasto-viscoplastic phase field modelling of anisotropic cleavage fracture

P. Shanthraj[a,b,*], B. Svendsen[a,d], L. Sharma[a,c], F. Roters[a], D. Raabe[a]

[a] Max-Planck-Institut für Eisenforschung, Max-Planck-Straße 1, 40237 Düsseldorf, Germany
[b] AICES, RWTH Aachen University, Schinkelstraße 2, 52062 Aachen, Germany
[c] Department of Mechanical Engineering, Eindhoven University of Technology, P.O. Box 513, 5600 MB Eindhoven, The Netherlands
[d] Material Mechanics, RWTH Aachen University, Schinkelstraße 2, 52062 Aachen, Germany

ARTICLE INFO

Keywords:
Phase field
Crystal plasticity
Anisotropic damage
Finite strain

ABSTRACT

A finite-strain anisotropic phase field method is developed to model the localisation of damage on a defined family of crystallographic planes, characteristic of cleavage fracture in metals. The approach is based on the introduction of an undamaged configuration, and the inelastic deformation gradient mapping this configuration to a damaged configuration is microstructurally represented by the opening of a set of cleavage planes in the three fracture modes. Crack opening is modelled as a dissipative process, and its evolution is thermodynamically derived. To couple this approach with a physically-based phase field method for brittle fracture, a scalar measure of the overall local damage is introduced, whose evolution is determined by the crack opening rates, and weakly coupled with the non-local phase field energy representing the crack opening resistance in the classical sense of Griffith. A finite-element implementation of the proposed model is employed to simulate the crack propagation path in a laminate and a polycrystalline microstructure. As shown in this work, it is able to predict the localisation of damage on the set of pre-defined cleavage planes, as well as the kinking and branching of the crack resulting from the crystallographic misorientation across the laminate boundary and the grain boundaries respectively.

1. Introduction

The failure of metals by cleavage has important consequences in a wide range of engineering applications (Curry and Knott, 1978; Beremin et al., 1983; Lu et al., 2000; Masolin et al., 2013), and identifying the microstructural features controlling cleavage fracture remains an area of intensive research (Wang et al., 2008; Koyama et al., 2013; Novak et al., 2010; Li and Baker, 2010; Kumar and Curtin, 2007). While the preference for metallic crystals to cleave on well defined crystallographic planes is supported by a large body of experimental work (Riedle et al., 1996; Joo et al., 2012; Kumar and Curtin, 2007), the percolation of these cracked crystallites across a heterogeneous microstructure, characterised by the presence of precipitates, grain and phase boundaries, is a process that occurs over several time and length scales, and is not well understood. Numerical simulations can potentially be used to reduce the multiscale complexity of the process and offer novel insights into the microstructural effects on material fracture (Bieler et al., 2009; Shanthraj and Zikry, 2013), however, the strongly anisotropic nature of cleavage fracture makes this a challenging task.

The topic of anisotropic damage has received considerable attention by the modelling community in the past decades. In the field of continuum damage mechanics, the earliest anisotropic models, developed by Dragon and Mroz (1979), Kachanov (1980), and

* Corresponding author at: Max-Planck-Institut für Eisenforschung, Max-Planck-Straße 1, 40237 Düsseldorf, Germany.
E-mail address: p.shanthraj@mpie.de (P. Shanthraj).

http://dx.doi.org/10.1016/j.jmps.2016.10.012
Received 30 June 2016; Received in revised form 18 October 2016; Accepted 31 October 2016
Available online 11 November 2016

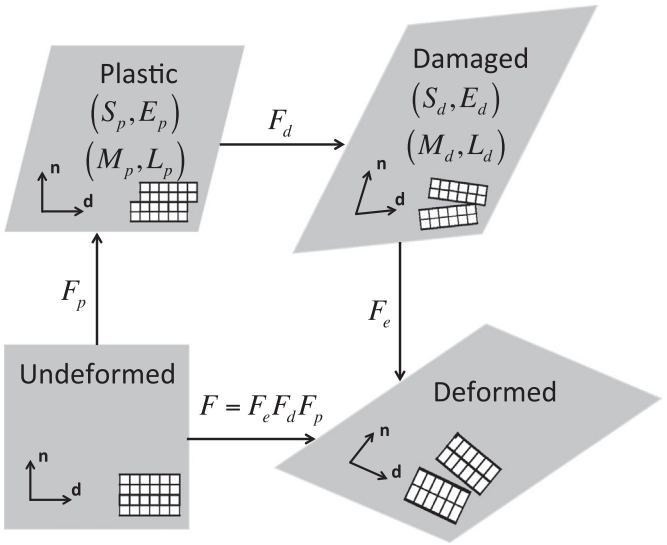

Fig. 1. Multiplicative decomposition of the deformation gradient, $\mathbf{F}$. The plastic deformation gradient, $\mathbf{F}_\mathrm{p}$, relating the undeformed configuration to the plastically deformed configuration, the damage deformation gradient, $\mathbf{F}_\mathrm{d}$, relating the plastically deformed configuration to the damaged configuration, and the elastic deformation gradient, $\mathbf{F}_\mathrm{e}$, relating the damaged configuration to the deformed configuration.

Murakami (1988), represent the damage as a second order tensor. However, the anisotropy of families of cleavage planes with a higher order of crystal symmetry cannot be represented by a second order tensor. Formulations using higher order tensors exist (Chaboche, 1992; Simo and Ju, 1987), but come at the cost of an increasing number of state variables. In the microplane theory (Carol and Bazant, 1997; Bazant and Prat, 1988), damage is considered locally on a set of predefined cleavage planes. This method, however, suffers from the drawback that a damaged stress tensor cannot uniquely be constructed from a set of damaged tractions on the individual planes. Furthermore, all these models are phenomenological, and the corresponding simulations must rely on empirically fitted rather than on physically-derived and unique single crystal parameters.

In recent years, the phase field method has emerged as a powerful and versatile tool in the modelling of brittle fracture (Bourdin et al., 2000; Miehe et al., 2010; Shanthraj et al., in press). The phase field model (PFM) for damage is based on the recently developed variational theory of brittle fracture by Bourdin et al. (2008), which is an extension of the classical theory of Griffith. However, with the exception of Clayton and Knap (2015, 2016) and Li et al. (2015), these extensions are isotropic in nature. Incorporating anisotropic interface evolution in PFMs can be achieved by using a tensorial surface energy in higher order PFMs, or through the introduction of an orientation dependent mobility (McFadden et al., 1993), both of which are less efficient than their isotropic counterpart owing to the increased computational cost.

In the current work, a finite-strain anisotropic PFM is developed to model the localisation of damage on a pre-defined family of crystallographic planes. The approach is based on the introduction of an undamaged configuration (Ekh et al., 2004; Menzel et al., 2002), and the corresponding inelastic deformation gradient mapping this configuration to a damaged configuration. The evolution of the damage deformation gradient is modelled by the opening of a set of cleavage planes in the three fracture modes, the evolution of which is thermodynamically formulated similar to the approach of Aslan et al. (2011). To couple this approach with a PFM for brittle fracture, a scalar measure of the overall local damage is introduced, whose evolution is determined by the crack opening rates, and weakly coupled to the non-local phase field energy representing the crack opening resistance in the classical sense of Griffith.

This paper is organised as follows: the derivation of the constitutive models and field equations is presented in Section 2, followed by an outline of their numerical implementation in Section 3. In Section 4 the results of two model problems are presented and discussed. A summary is provided in Section 5 along with perspectives for future applications.

2. Theory

2.1. Basic relations

Let $\mathcal{B}_0 \subset \mathbb{R}^3$ be a microstructural domain of interest, with boundary $\partial\mathcal{B}_0$. The deformation resulting from an applied loading defines a field $\chi(\mathbf{x})$: $\mathbf{x} \in \mathcal{B}_0 \rightarrow \mathbf{y} \in \mathcal{B}$ mapping points $\mathbf{x}$ in the undeformed configuration $\mathcal{B}_0$ to points $\mathbf{y}$ in the deformed configuration $\mathcal{B}$. The total deformation gradient, given by $\mathbf{F} = \partial\chi/\partial\mathbf{x} = \nabla\chi$, is multiplicatively decomposed as

$$\mathbf{F} = \mathbf{F}_\mathrm{e}\mathbf{F}_\mathrm{d}\mathbf{F}_\mathrm{p} \tag{1}$$

where $\mathbf{F}_\mathrm{p}$ is a lattice preserving isochoric mapping due to plastic deformation, $\mathbf{F}_\mathrm{d}$ is a lattice distorting mapping due to crack opening on a specified family of cleavage planes, and $\mathbf{F}_\mathrm{e}$ is a mapping to the deformed configuration (see Fig. 1). In the current approach the stress relaxation due to a damage process is captured through the stress-free deformation gradient, $\mathbf{F}_\mathrm{d}$. This is in contrast with

conventional PFMs for damage, where the damage stress relaxation is a result of a degradation of the material stiffness. Through such an approach, anisotropic damage can be easily modelled by constraining $\mathbf{F}_\mathrm{d}$ to evolve on a specified set of cleavage planes. Note that the order, $\mathbf{F} = \mathbf{F}_\mathrm{e}\mathbf{F}_\mathrm{d}\mathbf{F}_\mathrm{p}$, is adapted for purely numerical reasons as it defines lattice invariant plastic intermediate configuration.

Restricting attention to isothermal and quasi-static processes with no external supplies of momentum or energy, the balance relations for linear momentum, angular momentum, internal energy, and total entropy, are given by Šilhavý (1997)

$$\mathbf{0} = \mathrm{Div}\,\mathbf{P}, \quad \mathbf{F}\mathbf{P}^\mathrm{T} = \mathbf{F}^\mathrm{T}\mathbf{P}, \quad \dot{\varepsilon} = \mathbf{P}\cdot\dot{\mathbf{F}}, \quad \dot{\eta} = \delta/\theta, \tag{2}$$

Here, $\mathbf{P}$ is the first Piola-Kirchhoff stress, ε is the referential internal energy density, η is the referential entropy density, θ is the (constant) absolute temperature, and δ is the referential dissipation-rate density. Combination of $(2)_{3,4}$ yields the form

$$\delta = \mathbf{P}\cdot\dot{\mathbf{F}} - \dot{\psi} \tag{3}$$

for δ in terms of the referential free energy density $\psi := \varepsilon - \theta\eta$. The current model formulation is based on the basic constitutive form

$$\psi = \psi(\mathbf{F}, \mathbf{F}_\mathrm{p}, \mathbf{F}_\mathrm{d}, \boldsymbol{\xi}, \varphi, \nabla\varphi), \tag{4}$$

for ψ depending on a set $\boldsymbol{\xi}$ of local internal variables, the scalar damage phase field φ, and its gradient $\nabla\varphi$. Modelling $\mathbf{P}$ as purely energetic in this work, the hyperelastic relation

$$\mathbf{P} = \partial_\mathbf{F}\psi \tag{5}$$

holds. On the kinetic side, modelling φ as a non-conservative phase field, the (time-dependent) Ginzburg-Landau model

$$\dot{\varphi} = -M\delta_\varphi\psi \text{ in } \mathcal{B}_0, \quad \partial_{\nabla\varphi}\psi\cdot\mathbf{n} = 0 \text{ on } \partial\mathcal{B}_0^\mathrm{f}, \quad \dot{\varphi} = 0 \text{ on } \partial\mathcal{B}_0^\mathrm{k}, \tag{6}$$

(Allen and Cahn, 1979, e.g.,) applies assuming mixed no-flux, constant φ, boundary conditions. Here, M is the mobility, $\delta_x f := \partial_x f - \mathrm{Div}\,\partial_{\nabla x} f$ is the variational derivative, $\partial\mathcal{B}_0^\mathrm{k} \subset \partial\mathcal{B}_0$ represents the kinematic part, and $\partial\mathcal{B}_0^\mathrm{f} \subset \partial\mathcal{B}_0$ is the flux part, of $\partial\mathcal{B}_0 = \partial\mathcal{B}_0^\mathrm{k} \cup \partial\mathcal{B}_0^\mathrm{f}$. Together, (3)–(6) result in the residual form for the dissipation-rate density,

$$\delta = M(\delta_\varphi\psi)^2 - \partial_{\mathbf{F}_\mathrm{p}}\psi\cdot\dot{\mathbf{F}}_\mathrm{p} - \partial_{\mathbf{F}_\mathrm{d}}\psi\cdot\dot{\mathbf{F}}_\mathrm{d} - \partial_{\boldsymbol{\xi}}\psi\cdot\dot{\boldsymbol{\xi}} \tag{7}$$

2.2. Energetic constitutive relations

The free energy density (4) is modelled by the specific form

$$\psi(\mathbf{F}, \mathbf{F}_\mathrm{p}, \mathbf{F}_\mathrm{d}, \boldsymbol{\xi}, \varphi, \nabla\varphi) = \psi_\mathrm{e}(\mathbf{F}, \mathbf{F}_\mathrm{p}, \mathbf{F}_\mathrm{d}) + \varphi^2\psi_\mathrm{d}(\boldsymbol{\xi}) + \psi_\mathrm{I}(\varphi, \nabla\varphi) \tag{8}$$

Here, ψ_e represents the density of elastic stored energy in the undamaged material, ψ_d is the density of stored energy released during damage, and

$$\psi_\mathrm{I}(\varphi, \nabla\varphi) = \frac{c_{\mathrm{G}0}}{c_{\mathrm{H}0}}\frac{G_0}{l_0}(1-\varphi) + \frac{1}{c_{\mathrm{G}0}c_{\mathrm{H}0}}G_0 l_0|\nabla\varphi|^2 \tag{9}$$

represents the stored energy density of the interface between undamaged ($\varphi = 1$) and damaged ($\varphi = 0$) regions. As detailed in Shanthraj et al. (in press), ψ_I is scaled by the effective thickness, l_0, and energy density, G_0/l_0, of the interfacial region, and for the current dependence of ψ_I on φ, $c_{\mathrm{H}0} = 4/3$ and $c_{\mathrm{G}0} = \sqrt{2}$. In the context of brittle fracture, G_0 is associated with the fracture energy, and in the limit of a vanishing of l_0 this corresponds to classical Griffith fracture (Bourdin et al., 2000; Pham et al., 2011).

The elastic energy, ψ_e, is modelled here relative to the damaged configuration by the form

$$\psi_\mathrm{e}(\mathbf{F}, \mathbf{F}_\mathrm{d}, \mathbf{F}_\mathrm{p}) \equiv (\det\mathbf{F}_\mathrm{d})\psi_{\mathrm{ed}}(\mathbf{E}_\mathrm{d}, \mathbf{F}_\mathrm{d}) \tag{10}$$

in terms of the Green-Lagrange strain measure $\mathbf{E}_\mathrm{d} = \frac{1}{2}(\mathbf{F}_\mathrm{e}^\mathrm{T}\mathbf{F}_\mathrm{e} - \mathbf{I})$. Assuming that the work-conjugate 2nd Piola-Kirchhoff stress, $\mathbf{S}_\mathrm{d} := \partial_{\mathbf{E}_\mathrm{d}}\psi_{\mathrm{ed}} = \mathbf{0}$ at $\mathbf{E}_\mathrm{d} = \mathbf{0}$, and $|\mathbf{E}_\mathrm{d}| \ll 1$, the following quadratic representation

$$\psi_{\mathrm{ed}}(\mathbf{E}_\mathrm{d}, \mathbf{F}_\mathrm{d}) = \frac{1}{2}\mathbf{E}_\mathrm{d}\cdot\mathbb{C}_\mathrm{d}(\mathbf{F}_\mathrm{d})\mathbf{E}_\mathrm{d} \tag{11}$$

in terms of $\mathbf{E}_\mathrm{d}$ then holds, with the elastic stiffness relative to the damaged configuration, $\mathbb{C}_\mathrm{d}(\mathbf{F}_\mathrm{d}) := \partial_{\mathbf{E}_\mathrm{d}}\partial_{\mathbf{E}_\mathrm{d}}\psi_{\mathrm{ed}}(\mathbf{0}, \mathbf{F}_\mathrm{d})$. In the current approach, $\mathbb{C}_\mathrm{d}(\mathbf{F}_\mathrm{d})$ is modelled on the push-forward

$$\mathbb{C}_\mathrm{d}(\mathbf{F}_\mathrm{d}) := (\mathbf{F}_\mathrm{d}\square\mathbf{F}_\mathrm{d}^\mathrm{T})\mathbb{C}_\mathrm{p}(\mathbf{F}_\mathrm{d}^\mathrm{T}\square\mathbf{F}_\mathrm{d}) \tag{12}$$

(with $(\mathbf{A}\square\mathbf{B})\mathbf{C} := \mathbf{A}\mathbf{C}\mathbf{B}$) of the elastic stiffness with respect the plastical configuration, $\mathbb{C}_\mathrm{p}$, which is considered constant here as the crystal lattice is unaltered by plastic deformation. Note that the dependence of $\mathbb{C}_\mathrm{d}$ on $\mathbf{F}_\mathrm{d}$ in (12) is purely configurational and is not related to a damage mechanism. Substituting (12) into (11), results in the following reduced form for ψ_e

$$\psi_\mathrm{e}(\mathbf{F}, \mathbf{F}_\mathrm{d}, \mathbf{F}_\mathrm{p}) := \psi_{\mathrm{ep}}(\mathbf{E}_\mathrm{p}) = \frac{1}{2}\mathbf{E}_\mathrm{p}\cdot\mathbb{C}_\mathrm{p}\mathbf{E}_\mathrm{p} \tag{13}$$

In terms of the work conjugate stress-strain pair pulled back to the plastic configuration,

$$\mathbf{E}_\mathrm{p} = \mathbf{F}_\mathrm{d}^\mathrm{T}\mathbf{E}_\mathrm{d}\mathbf{F}_\mathrm{d} \quad \text{and} \quad \mathbf{S}_\mathrm{p} = \partial_{\mathbf{E}_\mathrm{p}}\psi_\mathrm{ep} = \mathbb{C}_\mathrm{p}\mathbf{E}_\mathrm{p} = \mathbf{F}_\mathrm{d}^{-1}\mathbf{S}_\mathrm{d}\mathbf{F}_\mathrm{d}^{-\mathrm{T}}\det\mathbf{F}_\mathrm{d} \tag{14}$$

The 1st Piola–Kirchhoff stress tensor, $\mathbf{P}$, is then related to $\mathbf{S}_\mathrm{p}$ through

$$\mathbf{P} = \mathbf{F}_\mathrm{e}\mathbf{F}_\mathrm{d}\mathbf{S}_\mathrm{p}\mathbf{F}_\mathrm{p}^{-\mathrm{T}}. \tag{15}$$

Details of the work conjugate relations are provided in Appendix B.

2.2.1. Crystal plasticity

The plastic deformation gradient is given in terms of the plastic velocity gradient, $\mathbf{L}_\mathrm{p}$, by the flow rule

$$\dot{\mathbf{F}}_\mathrm{p} = \mathbf{L}_\mathrm{p}\mathbf{F}_\mathrm{p} \tag{16}$$

where $\mathbf{L}_\mathrm{p}$ is work conjugate with the Mandel stress in the plastic configuration,

$$\mathbf{M}_\mathrm{p} = -\partial_{\mathbf{F}_\mathrm{p}}\psi\mathbf{F}_\mathrm{p}^\mathrm{T} = (\mathbf{F}_\mathrm{e}\mathbf{F}_\mathrm{d})^\mathrm{T}\mathbf{F}_\mathrm{e}\mathbf{F}_\mathrm{d}\mathbf{S}_\mathrm{p} \approx \mathbf{F}_\mathrm{d}^\mathrm{T}\mathbf{F}_\mathrm{d}\mathbf{S}_\mathrm{p}. \tag{17}$$

in the context of small elastic strains, i.e. $|\mathbf{E}_\mathrm{d}| \ll 1$. The crystal plasticity model used in the present study (for details see Roters et al., 2010), is an adoption of the phenomenological description of Peirce et al. (1983). The plastic velocity gradient $\mathbf{L}_\mathrm{p}$ is composed of the slip rates $\dot{\gamma}^\alpha$ on each of the slip systems, which are indexed by α.

$$\mathbf{L}_\mathrm{p} = \dot{\mathbf{F}}_\mathrm{p}\mathbf{F}_\mathrm{p}^{-1} = \sum_\alpha \dot{\gamma}^\alpha \mathbf{s}^\alpha \otimes \mathrm{n}^\alpha \tag{18}$$

where $\mathbf{s}^\alpha$ and $\in\alpha$ are unit vectors along the slip direction and slip plane normal, respectively. The plastic dissipation can then be reduced to the simpler slip system based conjugate pair

$$-\partial_{\mathbf{F}_\mathrm{p}}\psi\cdot\dot{\mathbf{F}}_\mathrm{p} = \sum_\alpha \tau^\alpha\dot{\gamma}^\alpha, \quad \text{where} \quad \tau^\alpha = \mathbf{M}_\mathrm{p}\cdot(\mathbf{s}^\alpha \otimes \mathrm{n}^\alpha). \tag{19}$$

The plasticity constitutive equations are given by,

$$\dot{\gamma}^\alpha = \dot{\gamma}_0 \left|\frac{\tau^\alpha}{g^\alpha}\right|^n \mathrm{sgn}(\tau^\alpha) \tag{20}$$

in terms of the reference shear rate $\dot{\gamma}_0$, and stress exponent n. The slip resistances on each slip system, g^α, evolve asymptotically towards g_∞ with shear γ^β $(\beta = 1,\ldots,12)$ according to the relationship

$$\dot{g}^\alpha = \dot{\gamma}^\beta h_0 \left|1 - g^\beta/g_\infty\right|^a \mathrm{sgn}(1 - g^\beta/g_\infty)h_{\alpha\beta} \tag{21}$$

with parameters h_0 and a. The interaction between different slip systems is captured by the hardening matrix $h_{\alpha\beta}$. On this basis, non-negativity of $\dot{\gamma}_0$, g_∞, h_0 and $h_{\alpha\beta}$ is sufficient to ensure non-negative plastic dissipation.

2.2.2. Damage

The damage deformation gradient is given in terms of the damage velocity gradient, $\mathbf{L}_\mathrm{d}$, by the flow rule

$$\dot{\mathbf{F}}_\mathrm{d} = \mathbf{L}_\mathrm{d}\mathbf{F}_\mathrm{d} \tag{22}$$

where $\mathbf{L}_\mathrm{d}$ is work conjugate with the Mandel stress in the damage intermediate configuration,

$$\mathbf{M}_\mathrm{d} = -\partial_{\mathbf{F}_\mathrm{d}}\psi\mathbf{F}_\mathrm{d}^\mathrm{T} = \mathbf{S}_\mathrm{d}\mathbf{F}_\mathrm{d}. \tag{23}$$

The damage velocity gradient, $\mathbf{L}_\mathrm{d}$, is composed of the crack opening rates of a set of cleavage planes, $\dot{o}_i^\alpha$, which are indexed by $\alpha = 1,\ldots,N_c$, in the three modes, $i = 1$, 2 and 3, illustrated in Fig. 2,

$$\mathbf{L}_\mathrm{d} = \dot{\mathbf{F}}_\mathrm{d}\mathbf{F}_\mathrm{d}^{-1} = \sum_{\alpha,i} \dot{o}_i^\alpha \mathbf{M}_i^\alpha \tag{24}$$

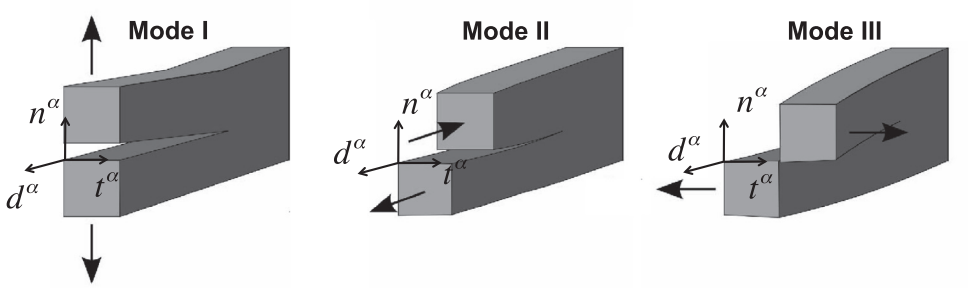

Fig. 2. Crack opening modes of a crystallographic cleavage system, α, represented in terms of its local coordinate system.

where, $\mathbf{M}_1^\alpha = \mathbf{n}^\alpha \otimes \mathbf{n}^\alpha$, $\mathbf{M}_2^\alpha = \mathbf{d}^\alpha \otimes \mathbf{n}^\alpha$ and $\mathbf{M}_2^\alpha = \mathbf{t}^\alpha \otimes \mathbf{n}^\alpha$ are the unit tensors of the different types of opening modes on cleavage plane α with local coordinate system $\mathbf{n}^\alpha$, $\mathbf{d}^\alpha$, and $\mathbf{t}^\alpha$. Taking $\boldsymbol{\xi} = \{o_i^\alpha\}$, the damage dissipation is given by

$$-\partial_{\mathbf{F}_\mathrm{d}}\psi \cdot \dot{\mathbf{F}}_\mathrm{d} - \partial_{\boldsymbol{\xi}}\psi \cdot \dot{\boldsymbol{\xi}} = \sum_{\alpha,i} \varsigma_i^\alpha \dot{o}_i^\alpha, \tag{25}$$

where

$$\varsigma_i^\alpha := \mathbf{M}_\mathrm{d} \cdot \mathbf{M}_i^\alpha - \varphi^2 \partial_{o_i^\alpha}\psi_\mathrm{D} = \mathbf{M}_\mathrm{d} \cdot \mathbf{M}_i^\alpha - \varphi^2 g_{cr} \tag{26}$$

represents the thermodynamic driving force conjugate to o_i^α, and the following simple form is assumed for the stored damage energy:

$$\psi_\mathrm{D} = \sum_{\alpha,i} g_{cr} o_i^\alpha \tag{27}$$

The evolution equations for the internal states are then given by the power law form

$$\dot{o}_i^\alpha = \dot{o}_0 \left| \frac{\langle \varsigma_i^\alpha \rangle}{\varphi^2 g_{cr}} \right|^p. \tag{28}$$

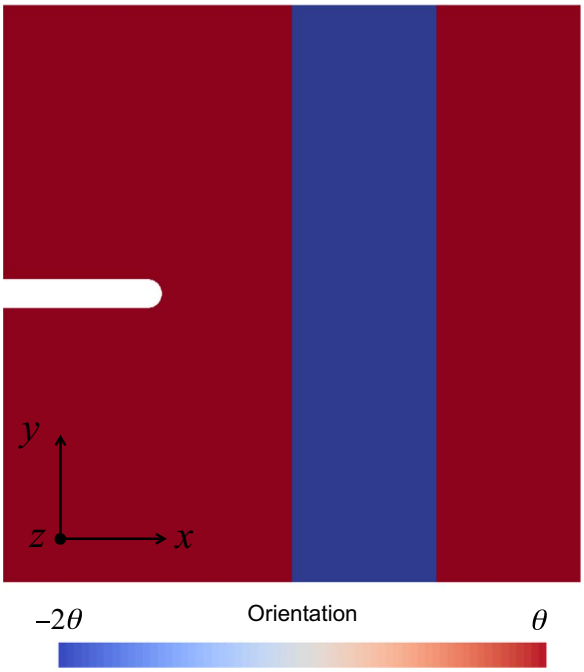

Fig. 3. A laminate plate with edge notch subject to uniaxial tension in the vertical direction. The crystallographic orientations, in terms of Euler angles (Bunge notation), of the individual lamellae are (θ°0°0°), (-2θ°0°0°) and (θ°0°0°) respectively.

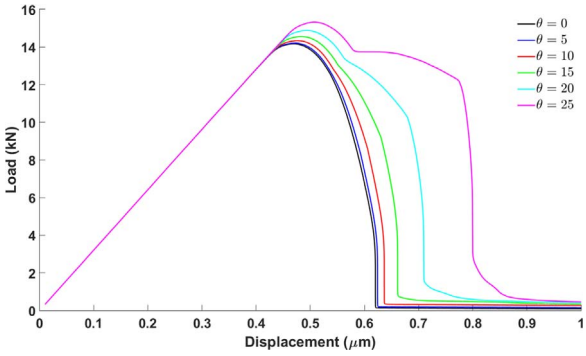

Fig. 4. Load-displacement curves for the notched elastic laminate plate subjected to uniaxial tension at different lamella orientations.

where the threshold operator, $\langle\cdot\rangle$, is used to reflect the sharp transition between damage and undamaged states. The non-negativity of $\dot{o}_0$ and g_{cr} is sufficient to ensure non-negative damage dissipation.

3. Numerical methods

3.1. Rate variational formulation of the initial boundary-value problems

Under certain conditions, the mechanical initial boundary-value problem (IBVP) can be formulated variationaly as the Euler-Lagrange relations of energy potentials. This was extended to a formulation of coupled IBVPs for history dependent extended continua as the stationarity conditions of energetic-kinetic rate potentials in, e.g., Svendsen (2004); Svendsen and Bargmann (2010) and Gladkov and Svendsen (2015). This approach is completely general and independent of any numerical considerations. However, for algorithmic and numerical solution purposes, it can be recast in incremental (i.e., time-integrated, semi-numerical) form. This fact has been exploited for example by Miehe and co-workers to formulate variational algorithms for a number of material models (Miehe et al., 2010; Miehe, 2011, 2014).

As detailed in Svendsen (2004), a rate-variational-based formulation of the IBVP is contingent in particular on the existence of a dissipation potential for the model in question. For the current model, we have the flux-based

$$d(\dot{\boldsymbol{\gamma}},\dot{\mathbf{o}},\dot{\varphi}) = \sum_{\alpha}\frac{g^{\alpha}\dot{\gamma}_0}{1/n+1}\left(\frac{|\dot{\gamma}^{\alpha}|}{\dot{\gamma}_0}\right)^{\frac{1}{n}+1} + \sum_{\alpha,i}\frac{\varphi^2 g_{\mathrm{cr}}\dot{o}_0}{1/p+1}\left(\frac{\dot{o}_i^{\alpha}}{\dot{o}_0}\right)^{\frac{1}{p}+1} + \frac{1}{2M}|\dot{\varphi}|^2 \tag{29}$$

form of this potential consistent with (6), (20) and (28). Besides this potential, the rate-variational formulation is based on the energy storage-rate density, ζ. For the current model, this is given by

$$\zeta(\nabla\dot{\boldsymbol{\chi}},\dot{\boldsymbol{\gamma}},\dot{\mathbf{o}},\dot{\varphi},\nabla\dot{\varphi}) = \mathbf{P}\cdot\nabla\dot{\boldsymbol{\chi}} - \sum_{\alpha}|\tau^{\alpha}\,\|\,\dot{\gamma}^{\alpha}| - \sum_{\alpha,i}\langle\varsigma_i^{\alpha}\rangle\dot{o}_i^{\alpha} + \partial_{\varphi}\psi\dot{\varphi} + \partial_{\nabla\varphi}\psi\cdot\nabla\dot{\varphi} \tag{30}$$

via the free energy density (4), the hyperelastic stress (5), as well as the evolution relations (20) and (28). Together, ζ and d determine the volumetric part of the rate functional

$$R = \int_{\mathcal{B}_0} r_{\mathrm{v}}\,\mathrm{d}\mathbf{x} + \int_{\partial\mathcal{B}_0^{\mathbf{f}}} r_{\mathrm{f}}\,\mathrm{d}\mathbf{s}, \quad \text{where} \quad r_{\mathrm{v}} = \zeta + d + r_{\mathrm{c}} \tag{31}$$

The additional contribution, $r_{\mathrm{c}} = \mu\dot{\varphi} + \lambda\dot{\varphi}$, enforces the constraints $\varphi \in [0,1]$, such that the complementarity relations, $\mu \le 0$, $\varphi \ge 0$, and $\mu\varphi = 0$ holds for the lower bound, and $\lambda \ge 0$, $\varphi \le 1$, and $\lambda\varphi = 0$ holds for the upper bound (Benson and Munson, 2006). The flux boundary conditions on $\partial\mathcal{B}_0^{\mathbf{f}}$ is given by r_{f}. In the context of (29) and (30), then, the first variation of R with respect to the rates is given by

$$\delta R = \int_{\mathcal{B}_0}\left\{\delta_{\dot{\boldsymbol{\chi}}} r_{\mathrm{v}}\cdot\delta\dot{\boldsymbol{\chi}} + \sum_{\alpha}\partial_{\dot{\gamma}^{\alpha}} r_{\mathrm{v}}\delta\dot{\gamma}^{\alpha} + \sum_{\alpha,i}\partial_{\dot{o}_i^{\alpha}} r_{\mathrm{v}}\delta\dot{o}_i^{\alpha} + \delta_{\dot{\varphi}} r_{\mathrm{v}}\delta\dot{\varphi}\right\}\mathrm{d}\mathbf{x} + \int_{\partial\mathcal{B}_0^{\mathbf{f}}}\{\partial_{\dot{\boldsymbol{\chi}}} r_{\mathrm{v}} + \partial_{\nabla\dot{\boldsymbol{\chi}}} r_{\mathrm{v}}\cdot\mathbf{n}\}\cdot\delta\dot{\boldsymbol{\chi}}\,\mathrm{d}\mathbf{s} + \int_{\partial\mathcal{B}_0^{\mathbf{f}}}\{\partial_{\dot{\varphi}} r_{\mathrm{v}} + \partial_{\nabla\dot{\varphi}} r_{\mathrm{v}}\cdot\mathbf{n}\}\delta\dot{\varphi}\mathrm{d}\mathbf{s} \tag{32}$$

Necessary conditions for δR vanishing in $\mathcal{B}_0$ are then

$$\begin{aligned}\mathbf{0} &= \delta_{\dot{\boldsymbol{\chi}}} r_{\mathrm{v}} = \delta_{\dot{\boldsymbol{\chi}}}\zeta = -\mathrm{Div}\,\mathbf{P},\ 0 = \partial_{\dot{\gamma}^{\alpha}} r_{\mathrm{v}} = \partial_{\dot{\gamma}^{\alpha}}\zeta + \partial_{\dot{\gamma}^{\alpha}} d = -\tau^{\alpha} + g^{\alpha}(|\dot{\gamma}^{\alpha}|/\dot{\gamma}_0)^{1/n}\,\mathrm{sgn}(\dot{\gamma}^{\alpha}),\ 0 = \partial_{\dot{o}_i^{\alpha}} r_{\mathrm{v}} = \partial_{\dot{o}_i^{\alpha}}\zeta + \partial_{\dot{o}_i^{\alpha}} d\\ &= -\langle\varsigma_i^{\alpha}\rangle + \varphi^2 g_{\mathrm{cr}}(\dot{o}_i^{\alpha}/\dot{o}_0)^{1/p},\ 0 = \delta_{\dot{\varphi}} r_{\mathrm{v}} = \delta_{\dot{\varphi}}\zeta + \delta_{\dot{\varphi}} d + \delta_{\dot{\varphi}} r_{\mathrm{c}} = \delta_{\varphi}\psi + \dot{\varphi}/M + \mu + \lambda,\end{aligned} \tag{33}$$

which is consistent with $(2)_1$, (20), (28) and the constrained form of (6), respectively, as well as the boundary conditions on $\partial\mathcal{B}_0^{\mathbf{f}}$

$$\mathbf{0} = \partial_{\dot{\boldsymbol{\chi}}} r_{\mathrm{f}} + \partial_{\nabla\dot{\boldsymbol{\chi}}} r_{\mathrm{v}}\cdot\mathbf{n} = -\mathbf{p}_{\mathrm{f}} + \partial_{\nabla\boldsymbol{\chi}}\psi\cdot\mathbf{n},\ 0 = \partial_{\dot{\varphi}} r_{\mathrm{f}} + \partial_{\nabla\dot{\varphi}} r_{\mathrm{v}}\cdot\mathbf{n} = 0 + \partial_{\nabla\varphi}\psi\cdot\mathbf{n}. \tag{34}$$

3.2. Finite element implementation

The rate-variational formulation yields the weak form of the field relations required for their finite-element (FE) implementation. In particular, Eq. (33) yields directly the weak momentum balance relation

$$\mathbf{0} = \int_{\mathcal{B}_0}\partial_{\nabla\dot{\boldsymbol{\chi}}} r\cdot\delta\nabla\dot{\boldsymbol{\chi}}\,\mathrm{d}\mathbf{x} + \int_{\partial\mathcal{B}_0^{\mathbf{f}}}\partial_{\dot{\boldsymbol{\chi}}} r_{\mathrm{f}}\cdot\delta\dot{\boldsymbol{\chi}}\,\mathrm{d}\mathbf{s} = \int_{\mathcal{B}_0}\nabla\delta\dot{\boldsymbol{\chi}}\cdot\mathbf{P}\mathrm{d}\mathbf{x} \tag{35}$$

where $\mathbf{p}_{\mathrm{f}} = \mathbf{0}$ is assumed for simplicity, and the weak Ginzburg-Landau relation

$$0 = \int_{\mathcal{B}_0}\delta_{\dot{\varphi}} r_{\mathrm{v}}\delta\dot{\varphi}\mathrm{d}\mathbf{x} = \int_{\mathcal{B}_0}\delta\dot{\varphi}\left[\frac{1}{M}\dot{\varphi} + 2\varphi\psi_{\mathrm{D}} - \frac{c_{\mathrm{G0}}}{c_{\mathrm{H0}}}\frac{G_0}{l_0} + \mu + \lambda\right]\mathrm{d}\mathbf{x} + \int_{\mathcal{B}_0}\nabla\delta\dot{\varphi}\cdot\frac{G_0 l_0}{c_{\mathrm{G0}}c_{\mathrm{H0}}}\nabla\varphi\mathrm{d}\mathbf{x} \tag{36}$$

where $\delta\dot{\boldsymbol{\chi}}$ and $\delta\dot{\varphi}$ are the virtual deformation and damage phase field rates respectively, such that $0 \le \delta\varphi \le 1$, and therefore $\mu\delta\dot{\varphi} + \lambda\delta\dot{\varphi} \le 0$. No-flux boundary conditions are assumed for the sake of simplicity.

The deformation field, $\boldsymbol{\chi}(\mathbf{x})$, and damage phase field, $\varphi(\mathbf{x})$, in addition to their virtual counterparts $\delta\boldsymbol{\chi}(\mathbf{x})$ and $\delta\varphi(\mathbf{x})$ are discretised using a FE basis of shape functions, $N_i^{\boldsymbol{\chi}}$, N_i^{φ}, $N_i^{\delta\boldsymbol{\chi}}$, and $N_i^{\delta\varphi}$, where, $\widetilde{\boldsymbol{\chi}}_i$, $\widetilde{\varphi}_i$, $\widetilde{\delta\boldsymbol{\chi}}_i$, and $\widetilde{\delta\varphi}_i$ are the respective degrees of freedom The corresponding discrete differential operator matrices are $\mathbf{B}_i^{\boldsymbol{\chi}}$, $\mathbf{B}_i^{\varphi}$, $\mathbf{B}_i^{\delta\boldsymbol{\chi}}$, and $\mathbf{B}_i^{\delta\varphi}$. Under these approximations, the weak forms Eqs. (35) and (36) can be rewritten as

$$\sum_i \widetilde{\delta\boldsymbol{\chi}}_i^T \int_{\mathcal{B}_0} [\mathbf{B}_i^{\delta\boldsymbol{\chi}}]^T \widetilde{\mathbf{P}} \mathrm{d}\mathbf{x} = \sum_i \widetilde{\delta\boldsymbol{\chi}}_i^T \mathcal{R}_{\mathrm{mech,i}} = \mathbf{0}. \tag{37}$$

and

$$\sum_i \widetilde{\delta\varphi}_i^T \int_{\mathcal{B}_0} [N_i^{\delta\varphi}]^T \left[\frac{N_i^{\varphi}\widetilde{\varphi}_i}{M} + 2\psi_{\mathrm{D}} N_i^{\varphi}\widetilde{\varphi}_i - \frac{c_{\mathrm{G0}}}{c_{\mathrm{H0}}}\frac{G_0}{l_0} \right] \mathrm{d}\mathbf{x} + \sum_i \widetilde{\delta\varphi}_i^T \int_{\mathcal{B}_0} [\mathbf{B}_i^{\delta\varphi}]^T \frac{G_0 l_0}{c_{\mathrm{G0}} c_{\mathrm{H0}}} \mathbf{B}_i^{\varphi}\widetilde{\varphi}_i \mathrm{d}\mathbf{x} = \sum_i \widetilde{\delta\varphi}_i^T \mathcal{R}_{\mathrm{dam,i}} \geq 0 \tag{38}$$

which defines a non-linear system of equations for the unknowns $(\widetilde{\boldsymbol{\chi}}_i, \widetilde{\varphi}_i)$. A time-discrete system of equations is obtained by using a backward Euler approximation

$$\dot{\widetilde{\varphi}} = \frac{\widetilde{\varphi}(t_n) - \widetilde{\varphi}(t_{n-1})}{\Delta t} \tag{39}$$

of the rate $\dot{\widetilde{\varphi}}$ in Eq. (38). Furthermore, irreversibility of the damage process can be enforced in the time discrete setting by modifying the upper bound constraint such that $0 \leq \widetilde{\varphi}_i(t_n) \leq \widetilde{\varphi}_i(t_{n-1})$.

The solution approach followed in this work involves solving the coupled system of Eqs. (37) and (38) within a staggered iterative loop until a self consistent solution is achieved for a time increment. The procedure is detailed in Algorithm 1. The advantage of such a staggered approach is that the solution scheme of each field can be described independently. The mechanical equilibrium Eq. (37) is solved using an inexact NEWTON method with a critical point secant line search (Eisenstat et al., 1994). Within each NEWTON iteration, a flexible GMRES linear solver (Saad, 1993) preconditioned with a smoothed-aggregation algebraic multigrid method (Vaněk et al., 1996) is used for the linear solve.

The variation inequality (38) for the evolution of the phase field variable is solved using the reduced space Newton method (Benson and Munson, 2006). In this approach, the phase field system is partitioned into sets composed of degrees of freedom on which the upper and lower bound constraints are active, respectively $\mathcal{A}_+$ and $\mathcal{A}_-$, given by

$$\mathcal{A}_+(t_n) = \{i | \widetilde{\varphi}_i(t_n) \geq \widetilde{\varphi}_i(t_{n-1}) \quad \text{and} \quad \mathcal{R}_{\mathrm{dam,i}} \leq 0\} \tag{40}$$

$$\mathcal{A}_-(t_n) = \{i | \widetilde{\varphi}_i(t_n) \leq 0 \quad \text{and} \quad \mathcal{R}_{\mathrm{dam,i}} \geq 0\} \tag{41}$$

and their complement, the inactive set, $\mathcal{I}$, composed of the phase field degrees of freedom on which the upper and lower bound constraints are inactive. Within each Newton iteration, a reduced system consisting the degrees of freedom belonging to the inactive set is solved using direct factorisation.

Algorithm 1. Staggered algorithm for field solution.

Data: $[\boldsymbol{\chi}]_{t_{n-1}}$, $[\varphi]_{t_{n-1}}$
Result: $[\boldsymbol{\chi}]_{t_n}$, $[\varphi]_{t_n}$
Initialisation:

$$[\varphi]_{t_n}^0 = [\varphi]_{t_{n-1}},$$
$$[\boldsymbol{\chi}]_{t_n}^0 = [\boldsymbol{\chi}]_{t_{n-1}},$$
$$j = 1$$

while $\| [\varphi]_{t_n}^j - [\varphi]_{t_n}^{j-1} \|_2 \geq tol_{\varphi}, \| [\boldsymbol{\chi}]_{t_n}^j - [\boldsymbol{\chi}]_{t_n}^{j-1} \|_2 \geq tol_{\boldsymbol{\chi}}$ **do**
  Solve $\mathcal{R}_{\mathrm{mech}}([\boldsymbol{\chi}]_{t_n}^j, [\varphi]_{t_n}^{j-1}) = 0$ for $[\boldsymbol{\chi}]_{t_n}^j$;
  Solve $\mathcal{R}_{\mathrm{dam}}([\boldsymbol{\chi}]_{t_n}^j, [\varphi]_{t_n}^j) = 0$ for $[\varphi]_{t_n}^j$;
  $j = j+1$
end

$$[\varphi]_{t_n} = [\varphi]_{t_n}^j,$$
$$[\boldsymbol{\chi}]_{t_n} = [\boldsymbol{\chi}]_{t_n}^j$$

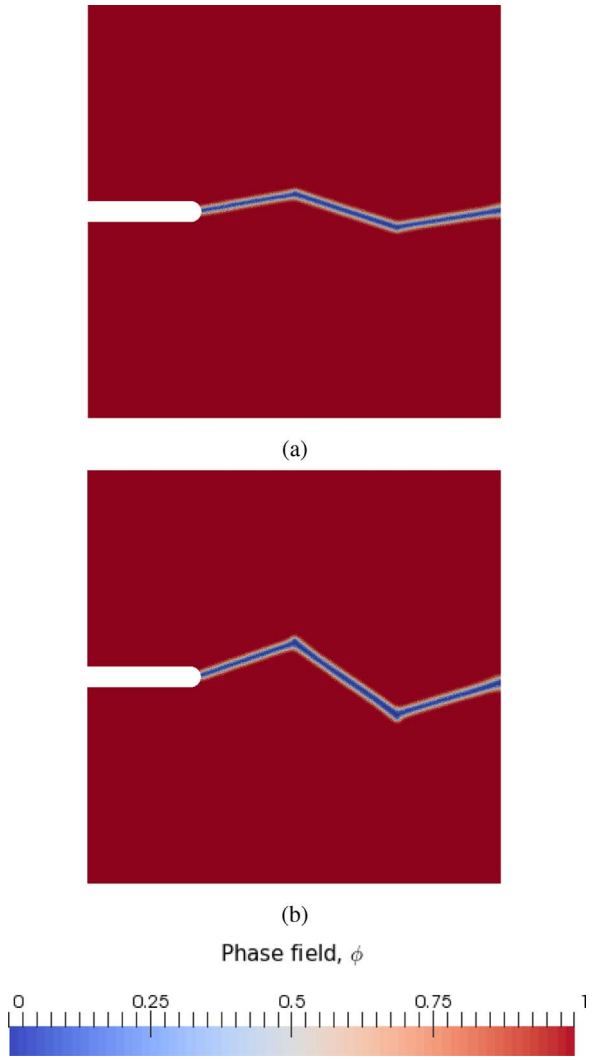

Fig. 5. The final damage phase field distribution in the notched elastic laminate plate subjected to uniaxial tension using (a) $\theta = 10°$ and (b) $\theta = 20°$. A damage phase field value of 0 corresponds to a fully opened crack while 1 refers to fully coherent bulk matter.

3.3. Constitutive stress integration

To obtain the stress, $\mathbf{P}$, resulting from a deformation, $\mathbf{F}$, a partitioning of $\mathbf{F}$, given by Eq. (1), is required. This non-linear problem is approached by first solving for the kinematic quantities, i.e. $\mathbf{F}_e$, $\mathbf{F}_d$, and $\mathbf{F}_p$, that is consistent with the resulting stress $\mathbf{P}$, for a frozen internal state of the material, followed by the evolution of the internal state variables using the updated kinematic quantities. This approach is repeated in a staggered manner till a solution for the kinematic quantities that is consistent with the current internal state variables is obtained.

The kinematic quantities, at a frozen internal state, are obtained by integrating the flow rules, given by Eqs. (16) and (22), over the time interval, $\triangle t$, using backward Euler time stepping, as

$$\mathbf{F}_p(t_0 + \triangle t) = [\mathbf{I} - \triangle t \mathbf{L}_p(\mathbf{M}_p)]^{-1} \mathbf{F}_p(t_0) \tag{42}$$

$$\mathbf{F}_d(t_0 + \triangle t) = [\mathbf{I} - \triangle t \mathbf{L}_d(\mathbf{M}_d)]^{-1} \mathbf{F}_d(t_0) \tag{43}$$

and, dropping the current time argument for brevity,

$$\mathbf{F}_e = \mathbf{F}\mathbf{F}_p^{-1}\mathbf{F}_d^{-1} \tag{44}$$

which represents an implicit system of equations as the stresses, $\mathbf{M}_p$ and $\mathbf{M}_d$, further depend on the kinematic quantities. A two-level iterative predictor-corrector scheme for $\mathbf{L}_p$ and $\mathbf{L}_d$, is used based on minimising the following residuals

$$\mathbf{R}_\mathrm{p} = \widetilde{\mathbf{L}}_\mathrm{p} - \mathbf{L}_\mathrm{p}(\mathbf{M}_\mathrm{p}(\widetilde{\mathbf{L}}_\mathrm{p}, \widetilde{\mathbf{L}}_\mathrm{d})) \tag{45}$$

$$\mathbf{R}_\mathrm{d} = \widetilde{\mathbf{L}}_\mathrm{d} - \mathbf{L}_\mathrm{d}(\mathbf{M}_\mathrm{d}(\widetilde{\mathbf{L}}_\mathrm{p}, \widetilde{\mathbf{L}}_\mathrm{d})). \tag{46}$$

The coupled system of Eqs. (45) and (46) is solved, using a Newton method, within a staggered iterative loop, until a consistent solution for $\widetilde{\mathbf{L}}_\mathrm{p}$ and $\widetilde{\mathbf{L}}_\mathrm{d}$ is achieved for a time step. The deformation gradient partitioning, and consequently the stresses, can be obtained by substituting this solution back in to Eqs. (42) to (44). The internal state variables are then integrated for the updated kinematic quantities and stresses, using backward Euler time stepping as

$$\boldsymbol{\xi}(t_n) = \boldsymbol{\xi}(t_{n-1}) + \triangle t \dot{\boldsymbol{\xi}}(\mathbf{S}_\mathrm{p}, \mathbf{F}_\mathrm{p}, \mathbf{F}_\mathrm{d}, \mathbf{L}_\mathrm{p}, \mathbf{L}_\mathrm{d}) \tag{47}$$

The overall solution procedure is detailed in Algorithm 2.

Algorithm 2. Algorithm for stress integration.

Data: $[\mathbf{F}]_{t_n}, [\mathbf{F}_\mathrm{p}]_{t_{n-1}}, [\mathbf{F}_\mathrm{d}]_{t_{n-1}}, [\mathbf{F}_\mathrm{e}]_{t_{n-1}}, [\boldsymbol{\xi}]_{t_{n-1}}$
Result: $[\mathbf{F}_\mathrm{p}]_{t_n}, [\mathbf{F}_\mathrm{d}]_{t_n}, [\mathbf{F}_\mathrm{e}]_{t_n}, [\mathbf{S}_\mathrm{p}]_{t_n}, [\boldsymbol{\xi}]_{t_n}$

Initialisation:

$$[\boldsymbol{\xi}]^0_{t_n} = [\boldsymbol{\xi}]_{t_{n-1}},$$
$$[\widetilde{\mathbf{L}}_\mathrm{p}]^0_{t_n} = [\mathbf{L}_\mathrm{p}]_{t_{n-1}},$$
$$[\widetilde{\mathbf{L}}_\mathrm{d}]^0_{t_n} = [\mathbf{L}_\mathrm{d}]_{t_{n-1}},$$

i =1
State Integration: $\boldsymbol{\xi}$ loop:
while $\|[\boldsymbol{\xi}]^i_{t_n} - [\boldsymbol{\xi}]^{i-1}_{t_n}\| \geq \mathrm{tol}_{\boldsymbol{\xi}}$ **do**
  j = 1
  Stress Integration: $\mathbf{L}_\mathrm{d}$ loop:
  while $\|[\widetilde{\mathbf{L}}_d]^j_{t_n} - [\widetilde{\mathbf{L}}_d]^{j-1}_{t_n}\|_2 \geq \mathrm{tol}_{\mathbf{L}_d}$ **do**
    $[\mathbf{F}_\mathrm{d}]_{t_n} = \left(\mathbf{I} - \triangle t [\widetilde{\mathbf{L}}_\mathrm{d}]^{j-1}_{t_n}\right)^{-1} [\mathbf{F}_\mathrm{d}]_{t_{n-1}}$
    k = 1
    Stress Integration: $\mathbf{L}_\mathrm{p}$ loop:
    while $\|[\widetilde{\mathbf{L}_p}]^k_{t_n} - [\widetilde{\mathbf{L}_p}]^{k-1}_{t_n}\|_2 \geq \mathrm{tol}_{\mathbf{L}_p}$ **do**
      $[\mathbf{F}_\mathrm{p}]_{t_n} = \left(\mathbf{I} - \triangle t [\widetilde{\mathbf{L}}_\mathrm{p}]^{k-1}_{t_n}\right)^{-1} [\mathbf{F}_\mathrm{p}]_{t_{n-1}}$
      $[\mathbf{F}_\mathrm{e}]_{t_n} = [\mathbf{F}]_{t_n} [\mathbf{F}_\mathrm{p}^{-1}]_{t_n} [\mathbf{F}_\mathrm{d}^{-1}]_{t_n}$
      $[\mathbf{S}_\mathrm{p}]_{t_n} = f\left([\mathbf{F}_\mathrm{e}]_{t_n}, [\mathbf{F}_\mathrm{d}]_{t_n}\right)$
      $\mathbf{R}_\mathrm{p} = [\widetilde{\mathbf{L}}_\mathrm{p}]^{k-1}_{t_n} - \mathbf{L}_\mathrm{p}\left([\mathbf{S}_\mathrm{p}]_{t_n}, [\mathbf{F}_\mathrm{d}]_{t_n}\right)$
      $[\widetilde{\mathbf{L}}_\mathrm{p}]^k_{t_n} = [\widetilde{\mathbf{L}}_\mathrm{p}]^{k-1}_{t_n} - \left(\partial_{\widetilde{\mathbf{L}_\mathrm{p}}} \mathbf{R}_\mathrm{p}\right)^{-1} \mathbf{R}_\mathrm{p}$
      $k = k$+1
    end
    $\mathbf{R}_\mathrm{d} = [\widetilde{\mathbf{L}}_\mathrm{d}]^{j-1}_{t_n} - \mathbf{L}_\mathrm{d}\left([\mathbf{S}_\mathrm{p}]_{t_n}, [\mathbf{F}_\mathrm{d}]_{t_n}\right)$
    $[\widetilde{\mathbf{L}}_\mathrm{d}]^j_{t_n} = [\widetilde{\mathbf{L}}_\mathrm{d}]^{j-1}_{t_n} - \left(\partial_{\widetilde{\mathbf{L}}_\mathrm{d}} \mathbf{R}_\mathrm{d}\right)^{-1} \mathbf{R}_\mathrm{d}$
    $j = j$+1
  end
  $[\boldsymbol{\xi}]^i_{t_n} = [\boldsymbol{\xi}]_{t_{n-1}} + \triangle t \,.\, \dot{\boldsymbol{\xi}}\left([\mathbf{S}_\mathrm{p}]_{t_n}, [\boldsymbol{\xi}]^{i-1}_{t_n}\right)$
  $i = i$+1
end

4. Results and discussion

The FE implementation of the developed damage model is applied to investigate the anisotropic crack propagation path both in a laminate microstructure and in a polycrystalline model microstructure.

4.1. Notched laminate plate

A square plate of length 10 mm, containing a horizontal notch of length 2.5 mm and tip radius 0.5 mm, is subjected to uniaxial tension strain of 0.02% by prescribing a vertical displacement on the top and bottom boundaries. The plate consists of three

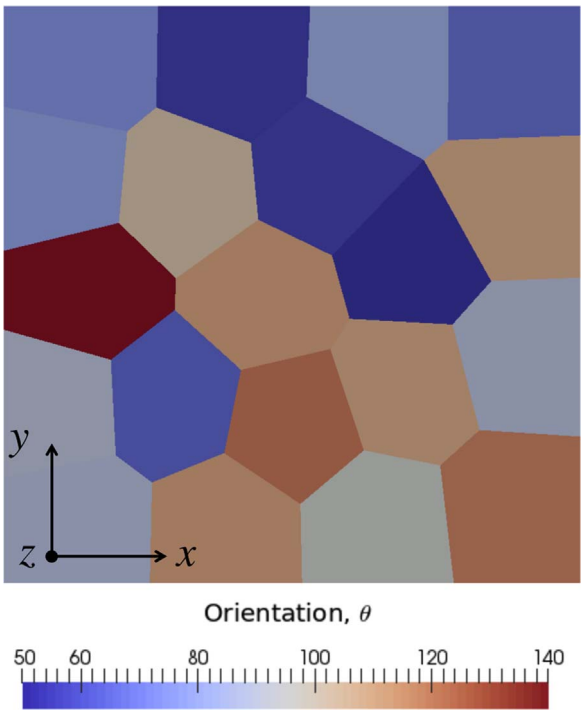

Fig. 6. Polycrystalline microstructure generated from a Voronoi tessellation of 20 randomly distributed seed points showing the initial orientation, (θ°0°0°), of the individual grains in the polycrystal.

crystallographically distinct lamellar regions having equal width ahead of the notch as illustrated in Fig. 3. The orientation of each crystal lamella, expressed as an Euler triplet (Bunge notation), is (θ°0°0°), (-2θ°0°0°) and (θ°0°0°) respectively, and cleavage in each crystal lamella is permitted only on the (010) plane. An isotropic elastic material model is used with elastic constants, C_{11} = 110.9 GPa and C_{12} = 58.4 GPa, interface energy, G_0 = 0.2 Jm^{-2}, interface width, l_0 = 0.1 mm, and critical fracture stress, g_{cr} = 10 MPa. The plate is meshed using Lagrange P2 elements elements having an element size of 0.05 mm.

To validate the anisotropic damage model, the above simulations are performed for values of θ ranging from 0° to 25° in

Table 1
Material parameters: elastic constants C_{ij}, reference shear rate $\dot{\gamma}_0$, stress exponent n, initial and saturation flowstress s_0 (or τ_0) and s_∞ (or τ_∞), hardening parameters a, h_0, and $h_{\alpha\beta}$, surface energy, G_0, characteristic length, l_0, damage mobility, M, critical traction for cleavage, g_{cr}, reference opening rate, $\dot{o}_0$, and damage rate sensitivity, p.

Parameter	Unit	Value
C_{11}	GPa	106.75
C_{12}	GPa	60.41
C_{44}	GPa	28.34
$\dot{\gamma}_0$	s^{-1}	0.001
n		20
g_0	MPa	31
g_∞	MPa	63
a		2.25
h_0	MPa	75
coplanar $h_{\alpha\beta}$		1
non-coplanar $h_{\alpha\beta}$		1.4
G_0	Jm^{-2}	0.085
l_0	μm	1.5
M	s^{-1}	0.01
g_{cr}	MPa	300
$\dot{o}_0$	s^{-1}	10
p		2

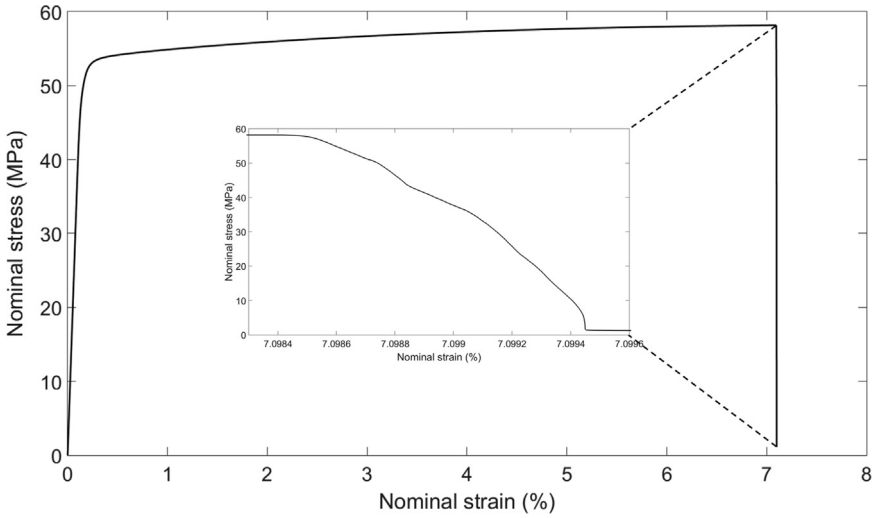

Fig. 7. Nominal stress-strain curve for the polycrystalline patch subjected to uniaxial tension, with an enlarged view of the unloading behaviour (inset).

increments of 5°. The corresponding load-displacement curves are shown in Fig. 4. Global unloading is observed to initiate at loads ranging from 14 kN, for $\theta = 0°$, to 15 kN, for $\theta = 25°$. The increase in critical load with lattice orientation results from the projection of the global stress state, i.e. uniaxial tensile stress, onto the rotated (010) plane. During the post-critical regime, a rapid initial unloading is observed, corresponding to crack propagation in the weaker initial laminate, and is followed by a hardening effect as the crack path is forced to kink abruptly by an angle of 3θ due to the lattice misorientation at the boundary with the stronger middle laminate. As the crack transitions to the last, weaker laminate further global softening is observed followed by complete structural failure. The alternating softening-hardening-softening effect of the laminate structure is more pronounced as the misorientation, i.e. θ, increases.

The local crack path for the case of a low angle ($\theta = 10°$) and high angle ($\theta = 20°$) laminate misorientation is shown in Fig. 5. It is verified that the anisotropic damage model is able to accurately predict the localisation of damage on the specified (010) planes in each laminate for the highly anisotropic case of the large-angle crack kinking across the multiple laminate boundaries.

4.2. Polycrystalline model microstructure

To study crack nucleation phenomena in more complex engineering materials, the developed damage model is applied to study the deformation and failure of a plastically deforming polycrystalline model material. The polycrystalline patch used, shown in Fig. 6, was generated by a Voronoi tessellation of 20 seed points randomly distributed within a square domain of length 1 mm. The individual grains were randomly misoriented about the z-axis, and the initial orientation of different grains is shown in Fig. 6. Cleavage in each grain is permitted only on the {100} family of planes as often observed in metals and alloys. A uniform simplex mesh of the polycrystalline patch was then generated, resulting in a uniform mesh with an average element size of 1.5 μm. Lagrange P2 and P1 elements were used to discretise the deformation and damage phase fields respectively. The patch is subjected to a uniaxial tensile strain rate of 0.01 s^{-1} by prescribing a vertical displacement on the top and bottom boundaries, while keeping the horizontal displacement on the left boundary fixed, up to a final time of 10 s. The phenomenological crystal plasticity constitutive model described in Section 2.2.1 for FCC Aluminium with twelve $\{111\} < -110>$ slip sytems is used, and the material parameters are listed in Table 1 (Shanthraj et al., 2015).

The nominal stress-strain curve is shown in Fig. 7. The material is observed to plastically deform at a global yield stress between 55 and 60 MPa up to a nominal strain of 7%, followed by rapid unloading due to crack nucleation and propagation. An enlarged view of the unloading behaviour (inset in Fig. 7) shows variations in the unloading rates, which corresponds to the variations in the alignment of the {100} cleavage planes with the loading axis in the different grains. The von Mises stress, pressure and total accumulated plastic slip, prior to crack nucleation is shown in Fig. 8. Large stresses, with a maximum von Mises stress of 200 MPa and maximum pressure of 250 MPa correspond to regions of severe plastic deformation, with a maximum plastic strain of 2.0. Grain boundaries and junctions are most susceptible to damage initiation due to the incompatibility of the plastic deformation modes in the respective grains forming the junction, which results in large stresses.

Fig. 9 shows the evolution of the damage phase field at different stages of the fracture process. The crack nucleates at the free surface, where a large gradient in plastic slip leads to necking of the material, and grows into the lower grain along the (1 0 0) plane. Lattice rotation resulting from large deformations at the advancing crack tip causes a curvature of the crack path as the crack propagation is constrained to the rotated (1 0 0) plane. In addition to the smooth curvature of the crack path resulting from lattice rotations, abrupt kinking of the crack path is also observed on encountering jumps in the lattice orientation at the grain boundaries. These kinking events are correlated with the changes in the unloading rate observed in Fig. 7 (inset), similar in effect to the results in

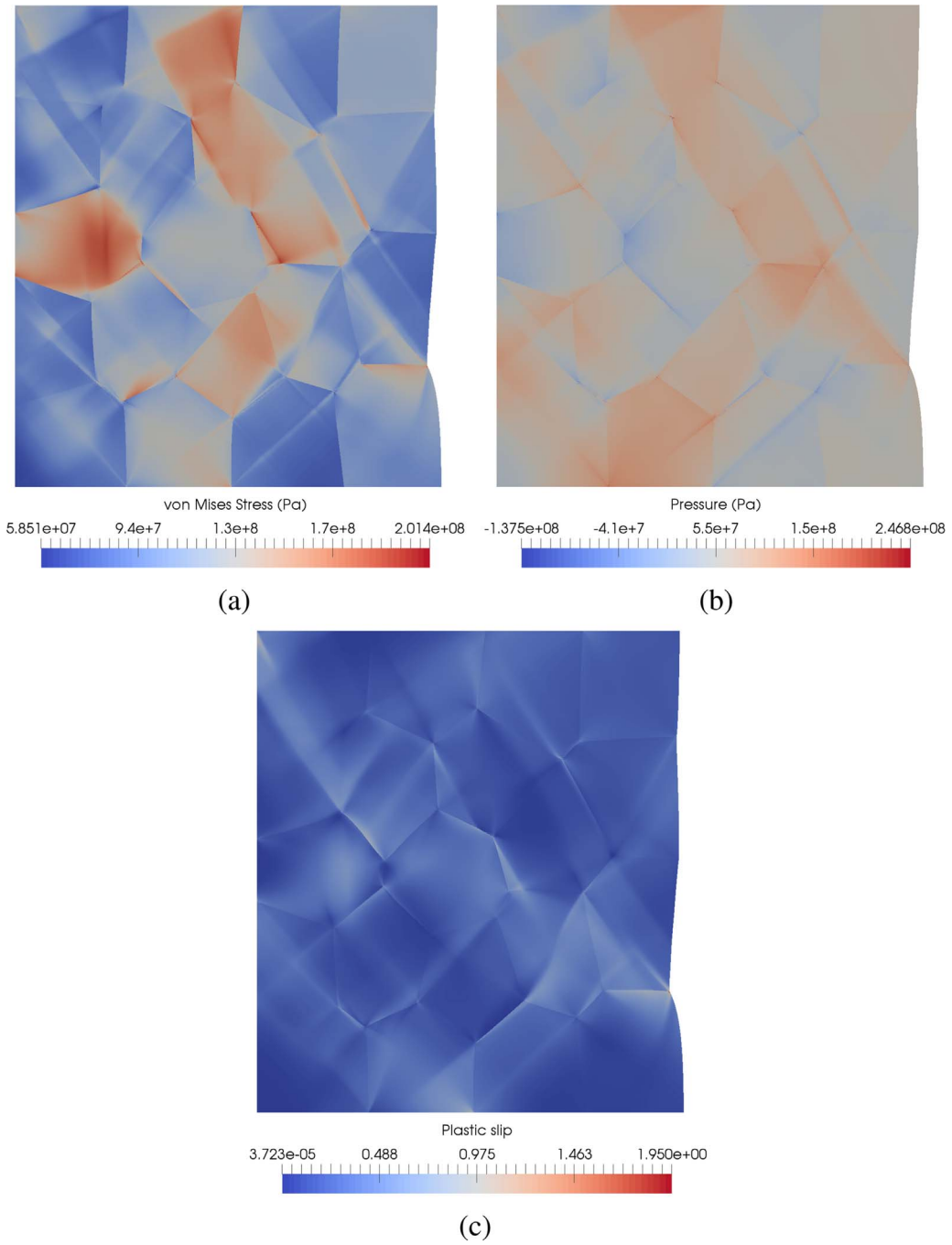

Fig. 8. (a) von Mises stress (b) hydrostatic pressure and (c) total accumulated plastic slip in a polycrystalline microstructure loaded to a nominal strain of 7% immediately prior to crack nucleation.

Section 4.1. Fig. 10 shows the corresponding evolution of the von Mises stress at different stages of the fracture process. The nucleation and growth of a crack is followed by an unloading of the material behind the crack tips and a general redistribution of the stress field ahead of the crack tip. However, as a result of extensive plastic deformation, a certain amount of residual stress remains in the unloaded material, and the residual stresses are larger in magnitude along the crack path due to the significant crack tip plasticity.

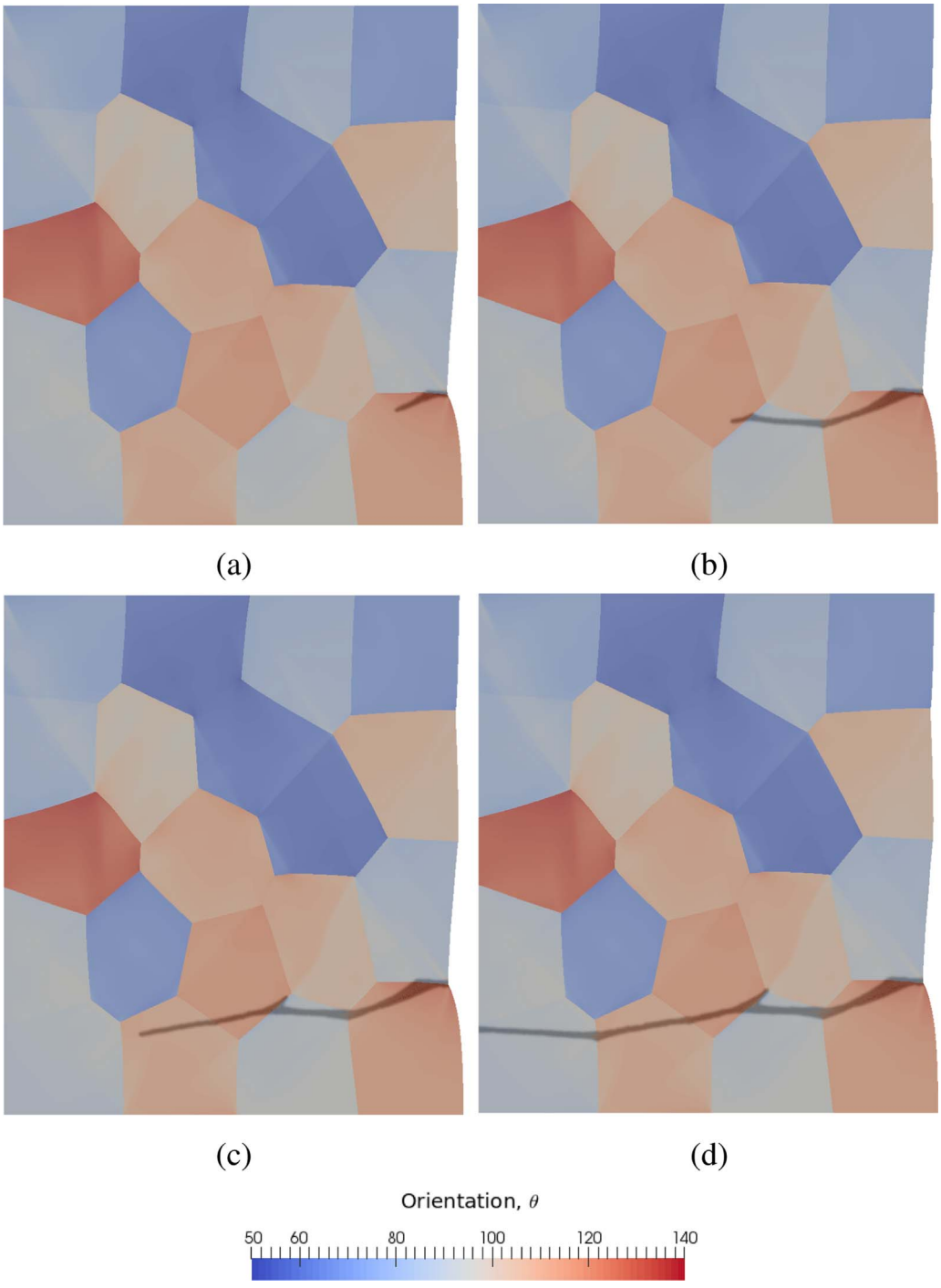

Fig. 9. Evolution of the damage phase field at different stages of the fracture process in a polycrystalline patch loaded loaded to a nominal strain of 7%. Fully damaged regions, i.e. $\varphi = 0$, are highlighted in black, and the colour scale indicates the in-plane orientation of the deformed lattice, (θ°0°0°). (For interpretation of the references to color in this figure legend, the reader is referred to the web version of this article.).

5. Conclusions

In the current work, a finite-strain anisotropic PFM is developed to model the localisation of damage on to a pre-defined family of crystallographic planes, characteristic of cleavage fracture in metals. The approach is based on the introduction of an undamaged configuration, and the inelastic deformation gradient mapping this configuration to a damaged configuration is microstructurally represented by the opening of a set of cleavage planes in the three fracture modes. The crack openings are modelled as a dissipative

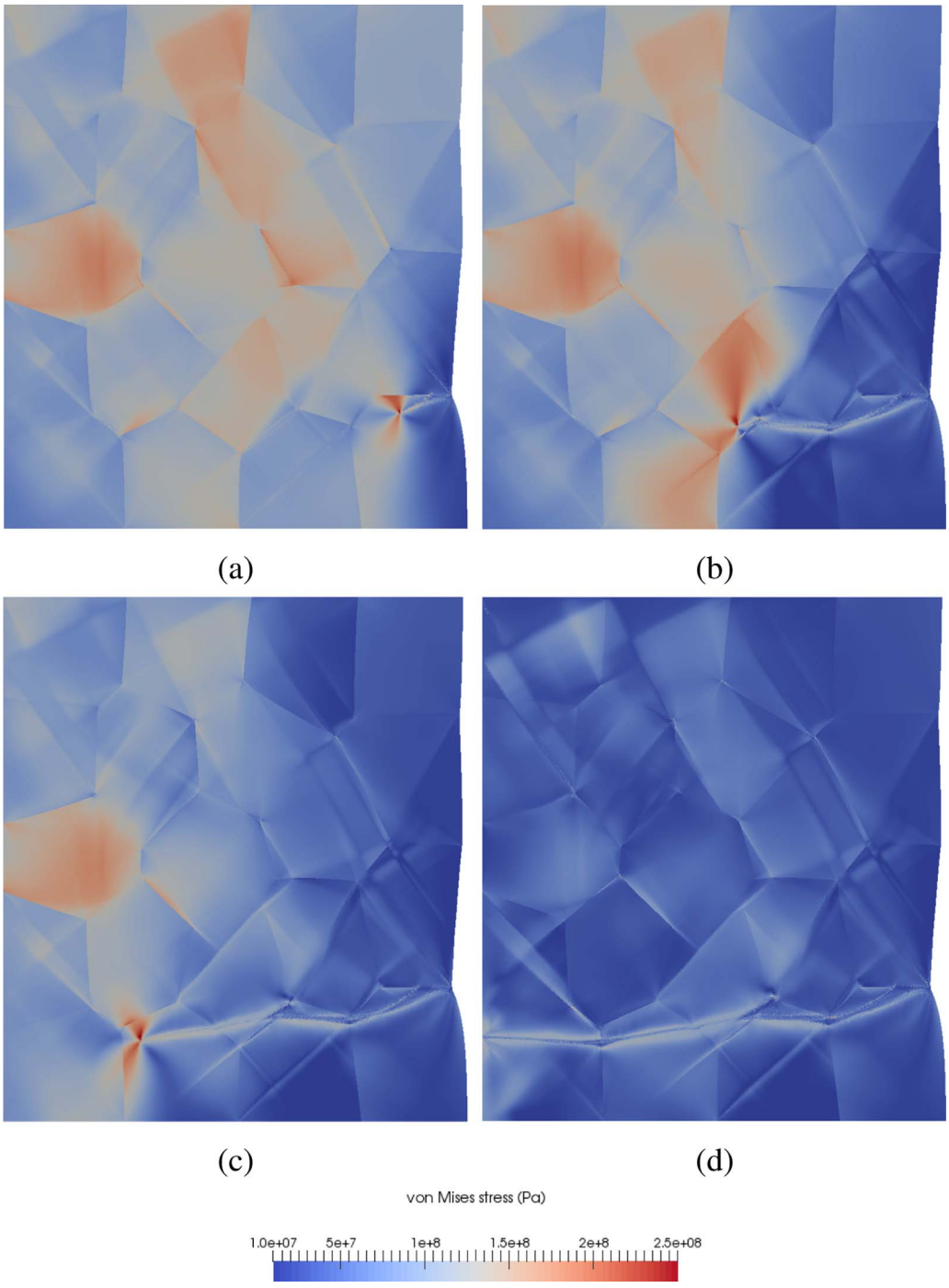

Fig. 10. Evolution of the von Mises stress at different stages of the fracture process in a polycrystalline patch loaded to a nominal strain of 7%.

process, and its evolution is thermodynamically derived. To couple this approach with a PFM for brittle fracture, a scalar measure of the overall local damage is introduced, whose evolution is determined by the crack opening rates, and weakly coupled with the non-local phase field energy representing the crack opening resistance in the classical sense of Griffith. The anisotropic damage PFM is discretised by a finite element method and applied to investigate the crack propagation path in a laminate and a polycrystalline microstructure. The proposed model is able to predict the localisation of damage on to the set of defined cleavage planes, as well as the kinking and branching of the crack resulting from the crystallographic misorientation across the laminate boundary and grain boundaries. The proposed method is capable of predicting complex crack patterns resulting from a rich set of interrelated driving forces, typically observed in the cleavage failure of engineering materials.

Appendix A. Notation

As a general scheme of notation, vectors are written as boldface lowercase letters (e.g. **a**, **b**), second-order tensors as boldface capital letters (e.g. **A**, **B**), and fourth-order tensors as blackboard-bold capital letters (e.g. $\mathbb{A}$, $\mathbb{B}$). For vectors and tensors, Cartesian components are denoted as, respectively, a_i, A_{ij} and A_{ijkl}. Second-order tensors are represented in this work as linear mappings between vectors and are denoted as **Ab** (in components $A_{ij}b_j$, implicit summation over repeated indices is used unless specified otherwise) and, likewise, fourth-order tensors represent linear mappings between second-order tensors and are designated as $\mathbb{A}\mathbf{B}$ ($A_{ijkl}B_{kl}$). The composition of two second-order tensors is denoted as **AB** ($A_{ik}B_{kj}$). The tensor (or dyadic) product between two vectors is denoted as $\mathbf{a} \otimes \mathbf{b}$ ($a_i b_j$). All inner products are indicated by a single dot between the tensorial quantities of the same order, e.g., $\mathbf{a}\cdot\mathbf{b}$ ($a_i b_i$) for vectors and $\mathbf{A}\cdot\mathbf{B}$ ($A_{ij}B_{ij}$) for second-order tensors. The transpose, $\mathbf{A}^{\mathrm{T}}$, of a tensor **A** is denoted by a superscript "T", and the inverse, $\mathbf{A}^{-1}$, by a superscript "−1". Additional notation is introduced where required.

Appendix B. Work conjugate relations

The total stress power, $\mathcal{P}$, can be split into elastic, damage and plastic contributions as

$$\mathcal{P} = \mathbf{P}\cdot\dot{F} = \underbrace{\mathbf{P}\cdot(\dot{\mathbf{F}}_{\mathrm{e}}\mathbf{F}_{\mathrm{d}}\mathbf{F}_{\mathrm{p}})}_{\mathcal{P}_{\mathrm{e}}} + \underbrace{\mathbf{P}\cdot(\mathbf{F}_{\mathrm{e}}\dot{\mathbf{F}}_{\mathrm{d}}\mathbf{F}_{\mathrm{p}})}_{\mathcal{P}_{\mathrm{d}}} + \underbrace{\mathbf{P}\cdot(\mathbf{F}_{\mathrm{e}}\mathbf{F}_{\mathrm{d}}\dot{\mathbf{F}}_{\mathrm{p}})}_{\mathcal{P}_{\mathrm{p}}} \tag{48}$$

The relation between $\dot{\mathbf{E}}_{\mathrm{p}}$ and $\mathbf{L}_{\mathrm{e}} = \dot{\mathbf{F}}_{\mathrm{e}}\mathbf{F}_{\mathrm{e}}^{-1}$ is obtained by taking the time derivative of Eq. (14). Under the assumption of small elastic strains, i.e. $\mathbf{F}_{\mathrm{e}}^{\mathrm{T}}\mathbf{F}_{\mathrm{e}} \approx \mathbf{I}$, this relation can be simplified to

$$\dot{\mathbf{E}}_{\mathrm{p}} = \frac{1}{2}\mathbf{F}_{\mathrm{d}}^{\mathrm{T}}\mathbf{F}_{\mathrm{e}}^{\mathrm{T}}(\mathbf{L}_{\mathrm{e}} + \mathbf{L}_{\mathrm{e}}^{\mathrm{T}})\mathbf{F}_{\mathrm{e}}\mathbf{F}_{\mathrm{d}}. \tag{49}$$

Using Eqs. (49) and (15), the elastic stress power term can be expressed in the plastic configuration to establish the work conjugacy between $\mathbf{S}_{\mathrm{p}}$ and $\mathbf{E}_{\mathrm{p}}$

$$\mathcal{P}_{\mathrm{e}} = \mathbf{P}\cdot(\mathbf{F}_{\mathrm{e}}^{-\mathrm{T}}\mathbf{F}_{\mathrm{d}}^{-\mathrm{T}}\dot{\mathbf{E}}_{\mathrm{p}}\mathbf{F}_{\mathrm{d}}^{-1}\mathbf{F}_{\mathrm{e}}^{-1}\mathbf{F}) = (\mathbf{F}_{\mathrm{d}}^{-1}\mathbf{F}_{\mathrm{e}}^{-1}\mathbf{P}\mathbf{F}_{\mathrm{p}}^{-\mathrm{T}})\cdot\dot{\mathbf{E}}_{\mathrm{p}} = \mathbf{S}_{\mathrm{p}}\cdot\dot{\mathbf{E}}_{\mathrm{p}} \tag{50}$$

Work conjugacy between $\mathbf{M}_{\mathrm{d}}$ and $\mathbf{L}_{\mathrm{d}}$ can be established by considering the damage stress power term and using Eq. $(14)_2$

$$\mathcal{P}_{\mathrm{d}} = \mathbf{P}\cdot(\mathbf{F}_{\mathrm{e}}\mathbf{L}_{\mathrm{d}}\mathbf{F}_{\mathrm{d}}\mathbf{F}_{\mathrm{p}}) = (\mathbf{F}_{\mathrm{d}}\mathbf{S}_{\mathrm{p}}\mathbf{F}_{\mathrm{d}}^{\mathrm{T}})\cdot\mathbf{L}_{\mathrm{d}} = \mathbf{M}_{\mathrm{d}}\cdot\mathbf{L}_{\mathrm{d}}\det\mathbf{F}_{\mathrm{d}} \tag{51}$$

Similarly, considering the plastic stress power, work conjugacy between $\mathbf{M}_{\mathrm{p}}$ and $\mathbf{L}_{\mathrm{p}}$ can be established

$$\mathcal{P}_{\mathrm{p}} = \mathbf{P}\cdot(\mathbf{F}_{\mathrm{e}}\mathbf{F}_{\mathrm{d}}\mathbf{L}_{\mathrm{p}}\mathbf{F}_{\mathrm{p}}) = (\mathbf{F}_{\mathrm{d}}^{\mathrm{T}}\mathbf{F}_{\mathrm{e}}^{\mathrm{T}}\mathbf{P}\mathbf{F}_{\mathrm{p}}^{\mathrm{T}})\cdot\mathbf{L}_{\mathrm{p}} = (\mathbf{F}_{\mathrm{d}}^{\mathrm{T}}\mathbf{F}_{\mathrm{d}}\mathbf{S}_{\mathrm{p}})\cdot\mathbf{L}_{\mathrm{p}} = \mathbf{M}_{\mathrm{p}}\cdot\mathbf{L}_{\mathrm{p}} \tag{52}$$

References

Allen, S.M., Cahn, J.W., 1979. A macroscopic theory for antiphase boundary motion and its application to antiphase domain coarsening. Acta Metall. 27, 1085–1095.
Aslan, O., Cordero, N., Gaubert, A., Forest, S., 2011. Micromorphic approach to single crystal plasticity and damage. Int. J. Eng. Sci. 49 (12), 1311–1325.
Bazant, Z.P., Prat, P.C., 1988. Microplane model for brittle-plastic material: I. theory. J. Eng. Mech. 114 (10), 1672–1688.
Benson, S.J., Munson, T.S., 2006. Flexible complementarity solvers for large-scale applications. Optim. Methods Softw. 21 (1), 155–168.
Beremin, F., Pineau, A., Mudry, F., Devaux, J.-C., DEscatha, Y., Ledermann, P., 1983. A local criterion for cleavage fracture of a nuclear pressure vessel steel. Metall. Trans. A 14 (11), 2277–2287.
Bieler, T., Eisenlohr, P., Roters, F., Kumar, D., Mason, D., Crimp, M., Raabe, D., 2009. The role of heterogeneous deformation on damage nucleation at grain boundaries in single phase metals. Int. J. Plast. 25 (9), 1655–1683, (Exploring New Horizons of Metal Forming Research).
Bourdin, B., Francfort, G.A., Marigo, J.J., 2000. Numerical experiments in revisited brittle fracture. J. Mech. Phys. Solids 48, 797–826.
Bourdin, B., Francfort, G.A., Marigo, J.-J., 2008. The variational approach to fracture. J. Elast. 91 (1–3), 5–148.
Carol, I., Bazant, Z.P., 1997. Damage and plasticity in microplane theory. Int. J. Solids Struct. 34 (29), 3807–3835.
Chaboche, J.-L., 1992. Damage induced anisotropy: on the difficulties associated with the active/passive unilateral condition. Int. J. Damage Mech. 1 (2), 148–171.
Clayton, J., Knap, J., 2015. Phase field modeling of directional fracture in anisotropic polycrystals. Comput. Mater. Sci. 98 (0), 158–169.
Clayton, J., Knap, J., 2016. Phase field modeling and simulation of coupled fracture and twinning in single crystals and polycrystals. Comput. Methods Appl. Mech. Eng..
Curry, D., Knott, J., 1978. Effects of microstructure on cleavage fracture stress in steel. Met. Sci. 12 (11), 511–514.
Dragon, A., Mroz, Z., 1979. A continuum model for plastic-brittle behaviour of rock and concrete. Int. J. Eng. Sci. 17 (2), 121–137.
Eisenstat, S.C., Walker, H.F., Eisenstatt, S.C., Homer, Walker, F., 1994. Choosing the forcing terms in an inexact newton method. SIAM J. Sci. Comput. 17, 16–32.
Ekh, M., Lillbacka, R., Runesson, K., 2004. A model framework for anisotropic damage coupled to crystal (visco) plasticity. Int. J. Plast. 20 (12), 2143–2159.
Gladkov, S., Svendsen, B., 2015. Thermodynamic and rate variational formulation of models for inhomogeneous gradient materials with microstructure and application to phase field modeling. Acta Mech. Sin. 31 (2), 162–172.
Joo, M., Suh, D.-W., Bae, J., Bhadeshia, H., 2012. Role of delamination and crystallography on anisotropy of charpy toughness in api-x80 steel. Mater. Sci. Eng.: A 546, 314–322.
Kachanov, M., 1980. Continuum model of medium with cracks. J. Eng. Mech. Div. 106 (5), 1039–1051.
Koyama, M., Akiyama, E., Tsuzaki, K., Raabe, D., 2013. Hydrogen-assisted failure in a twinning-induced plasticity steel studied under in situ hydrogen charging by electron channeling contrast imaging. Acta Mater. 61 (12), 4607–4618.
Kumar, S., Curtin, W.A., 2007. Crack interaction with microstructure. Mater. Today 10 (9), 34–44.
Li, B., Peco, C., Millán, D., Arias, I., Arroyo, M., 2015. Phase-field modeling and simulation of fracture in brittle materials with strongly anisotropic surface energy.

Int. J. Numer. Methods Eng. 102 (3–4), 711–727.
Li, Y., Baker, T.N., 2010. Effect of morphology of martensite-austenite phase on fracture of weld heat affected zone in vanadium and niobium microalloyed steels. Mater. Sci. Technol. 26 (9), 1029–1040.
Lu, Y., Wang, Q., Zeng, X., Ding, W., Zhai, C., Zhu, Y., 2000. Effects of rare earths on the microstructure, properties and fracture behavior of Mg-Ag alloys. Mater. Sci. Eng. A-Struct. Mater. Prop. Microstruct. Process. 278 (1–2), 66–76.
Masolin, A., Bouchard, P.-O., Martini, R., Bernacki, M., 2013. Thermo-mechanical and fracture properties in single-crystal silicon. J. Mater. Sci. 48 (3), 979–988.
McFadden, G., Wheeler, A., Braun, R., Coriell, S., Sekerka, R., 1993. Phase-field models for anisotropic interfaces. Phys. Rev. E 48 (3), 2016.
Menzel, A., Ekh, M., Steinmann, P., Runesson, K., 2002. Anisotropic damage coupled to plasticity: modelling based on the effective configuration concept. Int. J. Numer. Methods Eng. 54 (10), 1409–1430.
Miehe, C., 2011. A multi-field incremental variational framework for gradient-extended standard dissipative solids. J. Mech. Phys. Solids 59, 898–923.
Miehe, C., 2014. Variational gradient plasticity at finite strains. Part i: mixed potentials for the evolution and update problems of gradient-extended dissipative solids. Comput. Methods Appl. Mech. Eng. 268, 677–703.
Miehe, C., Welschinger, F., Hofacker, M., 2010. Thermodynamically consistent phase field models for fracture: variational principles and multi-field fe implementations. Int. J. Numer. Methods Eng. 83, 1273–1311.
Murakami, S., 1988. Mechanical modeling of material damage. J. Appl. Mech. 55 (2), 280–286.
Novak, P., Yuan, R., Somerday, B.P., Sofronis, P., Ritchie, R.O., 2010. A statistical, physical-based, micro-mechanical model of hydrogen-induced intergranular fracture in steel. J. Mech. Phys. Solids 58 (2), 206–226.
Peirce, D., Asaro, R., Needleman, A., 1983. Material rate dependence and localized deformation in crystalline solids. Acta Metall. 31 (12), 1951–1976.
Pham, K., Amor, H., Marigo, J.-J., Maurini, C., 2011. Gradient damage models and their use to approximate brittle fracture. Int. J. Damage Mech. 20 (4, SI), 618–652.
Riedle, J., Gumbsch, P., Fischmeister, H.F., 1996. Cleavage anisotropy in tungsten single crystals. Phys. Rev. Lett. 76 (19), 3594.
Roters, F., Eisenlohr, P., Hantcherli, L., Tjahjanto, D., Bieler, T., Raabe, D., 2010. Overview of constitutive laws, kinematics, homogenization and multiscale methods in crystal plasticity finite-element modeling: theory, experiments, applications. Acta Mater. 58 (4), 1152–1211.
Saad, Y., 1993. A flexible inner-outer preconditioned gmres algorithm. SIAM J. Sci. Comput. 14 (2), 461–469.
Shanthraj, P., Eisenlohr, P., Diehl, M., Roters, F., 2015. Numerically robust spectral methods for crystal plasticity simulations of heterogeneous materials. Int. J. Plast. 66, 31–45.
Shanthraj, P., Sharma, L., Svendsen, B., Roters, F., Raabe, D., 2016. A phase field model for damage in elasto-viscoplastic materials. Comput. Methods Appl. Mech. Eng.. http://dx.doi.org/10.1016/j.cma.2016.05.006.
Shanthraj, P., Zikry, M., 2013. Microstructurally induced fracture nucleation and propagation in martensitic steels. J. Mech. Phys. Solids 61 (4), 1091–1105.
Simo, J., Ju, J., 1987. Strain-and stress-based continuum damage modelsi. formulation. Int. J. Solids Struct. 23 (7), 821–840.
Svendsen, B., 2004. On the thermodynamic- and variational-based formulation of models for inelastic continua with internal lengthscales. Comput. Methods Appl. Mech. Eng. 48, 5429–5452.
Svendsen, B., Bargmann, S., 2010. On the continuum thermodynamic rate variational formulation of models for extended crystal plasticity at large deformation. J. Mech. Phys. Solids 58, 1253–1271.
Vaněk, P., Mandel, J., Brezina, M., 1996. Algebraic multigrid by smoothed aggregation for second and fourth order elliptic problems. Computing 56 (3), 179–196.
Šilhavý, M., 1997. The Mechanics and Thermodynamics of Continuous Media. Springer.
Wang, C., Wang, M., Shi, H., Hui, W., Dong, H., 2008. Effect of microstructural refinement on the toughness of low carbon martensitic steel. Scr. Mater. 58 (6), 492–495.